Supplementary

S1. Methods and materials

S1.1 Chemicals and reagents

The potassium iodide (KI, ≥99%), bismuth nitrate pentahydrate ($Bi(NO_3)_3 \cdot 5H_2O$, ≥99.99%), p-benzoquinone, and nitric acid (HNO_3), Dimethyl sulfoxide (DMSO) (≥99.9%) and vanadyl acetylacetonate ($VO(acac)_2$, 98%) utilized in this experiment were sourced from Sigma Aldrich. Fluorine-doped Tin Oxide (FTO, 25 × 25 × 2.0 mm) glass, obtained from Latech, served as the substrate for photoanode preparation. Before use, the substrate was cleaned with deionized water, acetone and ethanol for 20 minutes using sonication.

S1.2 Fabrication of $BiVO_4$

$BiVO_4$ photoanodes were fabricated on FTO substrates using an electrodeposition-annealing technique. The electrodeposition process was conducted using an electrochemical workstation (VMP3, Bio-logic, France) in a three-electrode configuration, with a cleaned FTO substrate as the working electrode, an Ag/AgCl electrode as the reference electrode, and a Pt foil as the counter electrode. The electrolyte for preparing nanoporous $BiVO_4$ consisted of 30 mL of 0.4 mol/L KI and 0.04 mol/L $Bi(NO_3)_3$ aqueous solution, combined with 30 mL of 0.23 mol/L p-benzoquinone ethanol solution. The pH of this mixture was adjusted to 1.7 using HNO_3. Electrodeposition at -0.1 V vs. Ag/AgCl for 10 minutes produced BiOI. This is used as a precursor to $BiVO_4$. Subsequently, the surface of BiOI was coated with 0.2 mol/L $VO(acac)_2$ DMSO solution and then annealed at 400°C for two and half hours with a heating rate of 2 °C/min. Following calcination, the $BiVO_4$ was immersed in a 0.5 mol/L NaOH solution for a few minutes to remove any residual V_2O_5.

S1.3 Characterizations

Photocatalyst morphology was characterized through field emission scanning electron microscopy (FESEM, JSM 6700F, JEOL, Japan), while the crystalline structure and

phase were evaluated using X-ray diffraction (XRD, Bruker AXS, Germany), with a scanning step of 0.02 degrees at a speed of 2.5 degrees/min. X-ray photoelectron spectroscopy (XPS) measurements were performed with a PHI 5400 system supplied by Physical Electronic Inc., which is equipped with a non-monochromatic Aluminium (Al)- Kα X-ray source (hν = 1486.7 eV). During XPS measurement, the system was operated at a power setting of 200 W with 13.5 kV accelerating electron voltage, where the analysis chamber was maintained at 10^{-9} mbar vacuum. The pass energy of the analyzer during XPS full survey measurement was set at 89.45 eV and at high resolution measurement was set at 71.55 eV. Thus obtained XPS high resolution spectra were peak shifted to neutralize the charging effect by referencing the adventitious carbon (C-C) bonding peak at 284.8 eV. Each measurement covers a circular analysis area that is 0.4 mm in diameter with an effective sampling depth of approximately 3–5 nm. Thus, all the obtained XPS spectra were processed using the MultiPak version 8.0 software issued by Physical Electronics Inc. UV-vis diffuse reflectance spectra (DRS) on a UV-2600 spectrophotometer (Shimazu, Japan), with $BaSO_4$ as a background, were used to assess optical properties.

S1.4 Photoelectrochemical performance

The photoelectrochemical (PEC) processes were performed within a three-electrode configuration, utilizing the synthesized photoanodes as the working electrode, an Ag/AgCl electrode as the reference, and a Pt foil as the counter electrode. Schematic of the setup shown in Schematic 1B. This PEC cell had a capacity of 100 mL, and the gap between the photoanode and cathode was 2.5 cm. TC-HCl was selected as model pollutant, introduced at a concentration of 10 ppm.

For the PEC experiments, an electrolyte solution was prepared, consisting of 100mL of 2mmol/L Na_2SO_4 at pH 7, with 10 mg/L of TC-HCl, which served as the typical condition. The applied potential was maintained at 1.0 V vs. Ag/AgCl throughout the experiments. The PEC reactions were conducted with constant stirring to ensure uniformity. Illumination was provided by a 300 W Xenon lamp (PLS-SXE300UV, Perfect Light Technology, Beijing) equipped with a UV cut-off filter allowing only

visible light ($\lambda \geq 400$ nm) to pass through. For comparison purposes, photocatalytic experiments were performed under identical conditions without applying an external voltage, and electrocatalytic experiments were conducted in the absence of visible light. Each experiment was repeated three times to ensure reproducibility, and the figures presented the average value. The levels of PPCPs were quantified using an Ultra-Performance Liquid Chromatography (UPLC) system (1260 series, Agilent Technologies, USA) that was equipped with a Zorbax SB-C18 (2.1 × 150 mm, particle size 3.5μm, Agilent) and a UV detector. The analysis employed a mobile phase composed of ACN/ultrapure water in a 20:80 (v/v %) ratio, with a flow rate of 1 mL/min.

The steady-state concentration of radicals was determined using a 0.008 mM solution, with nitrobenzene (NB), benzoic acid (BA), and 1,4-dimethoxybenzene (DMOB) employed as selective probes. These molecules were chosen for their ability to react specifically with different radical species, allowing for precise quantification and characterization of the reactive species present in the photoelectrochemical (PEC) system. By analyzing their interactions with the radicals, it became possible to identify the key contributors to the degradation process and better understand the system's overall performance (Eqs. (S1)-(S3)).

$$K_{NB} = K_{NB,\bullet OH}[\bullet OH]_{SS} \quad \text{(S1)}$$

$$K_{BA} = K_{BA,\bullet OH}[\bullet OH]_{SS} + K_{BA,\bullet Cl}[\bullet Cl]_{SS} \quad \text{(S2)}$$

$$K_{DMOB} = K_{DMOB,\bullet OH}[\bullet OH]_{SS} + K_{DMOB,\bullet Cl}[\bullet Cl]_{SS} + K_{DMOB,\bullet ClO}[\bullet ClO]_{SS} \quad \text{(S3)}$$

NB selectively reacts with •OH ($k_{NB,\bullet OH} = 3.9 \times 10^9$ L mol^{-1} s^{-1}), while BA reacts with both •OH and •Cl ($k_{BA,\bullet OH} = 5.9 \times 10^9$ L mol^{-1} s^{-1}; $k_{BA,\bullet Cl} = 1.8 \times 10^9$ L mol^{-1} s^{-1}), and DMOB reacts with •OH, •Cl, and •ClO ($k_{DMOB,\bullet OH} = 7.0 \times 10^9$ L mol^{-1} s^{-1}; $k_{DMOB,\bullet Cl} = 1.8 \times 10^{10}$ L mol^{-1} s^{-1}; $k_{DMOB,\bullet ClO} = 2.1 \times 10^9$ L mol^{-1} s^{-1}). The probe concentrations

were analyzed using HPLC system equipped with a C18 column. The mobile phase consisted of 60% methanol and 40% ultrapure water, with a flow rate of 1.0 mL/min. Detection wavelengths were set at 257 nm for nitrobenzene (NB), and 232 nm for both benzoic acid (BA) and 1,4-dimethoxybenzene (DMOB).

S1.5 HER (Hydrogen Evolution Reaction)

The photoelectrochemical (PEC) processes were performed within a three-electrode configuration, in a dual chamber H-cell, utilizing the synthesized photoanodes as the working electrode, an Ag/AgCl electrode as the reference, and a Pt foil as the counter electrode. Both chambers were purged with argon (Ar) gas to prevent oxygen-related side reactions. The evolution of hydrogen gas (H_2) during the PEC process was assessed through gas chromatography (GC) equipped with a thermal conductivity detector (TCD), where the oven, injector, and detector were set to temperatures of 60°C, 60°C, and 200°C, respectively. The electrochemical cell was filled with a synthetic ROC solution (0.002 mol/L Na_2SO_4+0.01 mol/L NaCl) at a pH of 7. All potentials were subsequently converted to the reversible hydrogen electrode (RHE) scale using the following equation (Eq. (S4)):

$$E_{RHE} = E^0_{Ag/AgCl} + E_{Ag/AgCl} + 0.059 \times pH \quad \text{(S4)}$$

Here, $E_{Ag/AgCl\ vs.\ NHE}$ is the reference potential for Ag/AgCl which is 0.197 V at 20°C. Electrochemical impedance spectroscopy (EIS) was performed under illumination at an open-circuit potential of 1.23 V vs. RHE, using an amplitude perturbation of 0.1 V across a frequency range of 100 kHz to 0.1 Hz, and chopped photocurrent densities were measured in 1.23 V vs. RHE.

The Applied Bias Photon-to-Current Efficiency (ABPE) for H_2 evolution by the photoanode was calculated using the following equation (Eq. (S5)):

$$ABPE(\%) = \frac{I \times (1.23 - V_{app})}{P_{incident}} \times 100$$

(S5)

Where, V_{app} represents the externally applied potential relative to the Reversible Hydrogen Electrode (RHE), I denotes the recorded current density, and $P_{incident}$ refers to the power density of the incident light, measured in $mWcm^{-2}$.

The charge separation efficiency (η_{sep}) represents the efficiency with which photogenerated electron-hole pairs are separated and transported to the reaction sites. It is calculated as (Eq. (S6)):

$$\eta_{sep} = \frac{J_{Na_2SO_3}}{J_{abs}}$$

(S6)

Where $J_{Na_2SO_3}$ is the photocurrent density measured in the presence of Na_2SO_3 as a hole scavenger and J_{abs} is the theoretical photocurrent density corresponding to the total absorbed photons. The charge injection efficiency (η_{inj}) represents the fraction of separated charge carriers that participate in the surface reaction (H_2 evolution) instead of recombining. It is calculated as (Eq. (S7)):

$$\eta_{inj} = \frac{J_{H_2O}}{J_{Na_2SO_3}}$$

(S7)

Where J_{H_2O} is the photocurrent density measured without the scavenger (actual photocurrent under water-splitting conditions).

S1.6 Sample post-treatment analysis of OMs

The distribution of molecular sizes for hydrophilic organic compounds was analyzed using a liquid chromatography-organic carbon detection (LC-OCD) system (DOC Labor Dr. Huber, Germany). The LC-OCD technique identifies five fractions, ordered from highest to lowest molecular weight: biopolymers (>>20,000 g/mol), humic

substances (~1,000 g/mol), building blocks (300-500 g/mol), low molecular weight (LMW) neutrals (<350 g/mol), and LMW acids (<350 g/mol).

Disinfection by-products (DBPs) in the samples were extracted according to established methods (USEPA, 551.1 for THMs and 552.3 for HAAs) and were quantified through gas chromatography with an electron capture detector and a capillary column (HP-5, 30 m × 0.32 mm inner diameter, 0.25 μm film thickness, Agilent, USA).

The toxicity for each disinfection byproduct (DBP) can be determined using eq. S8, which relates the concentration of each DBP, denoted as c(DBP), to its semi-lethal concentration, LC50 (mol/L) (LC50 is the concentration of each specific disinfection by-product (DBP) that leads to a 50% decrease in the growth of Chinese Hamster Ovary cells following 72 hours of exposure), and its relative molecular weight, M(DBP), as indicated in Table S1 (Xiang et al. 2020).

Table S1 Molecular weight and LC50 values of DBPs using the Chinese Hamster Ovary chronic cytotoxicity assay

	DBPs	M_w (g/mol)	LC_{50} (mol/L)	References
THMs	TCM	119.38	9.62×10^{-3}	(Plewa et al. 2010; Luo et al. 2020)
HANs	DCAN	109.94	5.73×10^{-5}	(Luo et al. 2020)
	TCAN	144.38	1.60×10^{-4}	
	MCAA	94.5	8.1×10^{-4}	
HAAs	DCAA	128.94	7.3×10^{-3}	(Plewa et al. 2010; Luo et al. 2020)
	TCAA	163.38	2.4×10^{-3}	

$$Cytotoxicity = \frac{c(DBP)/M(DBP)}{LC_{50}} \quad \text{(S8)}$$

Table S2 Characteristics of synthetic ROC

Parameter	Value	Unit
Conductivity	1.68	mS
TDS	840	mg/L
pH	7.5	-
Alkalinity	230	mg $CaCO_3$/L
TOC	12	mg/L
UV_{254}	0.38	cm^{-1}
Cl^-	300	mg/L
SO_4^{2-}	200	mg/L
NO_3^-	60	mg/L
PO_4^{3-}	20	mg/L
Na^+	320	mg/L
K^+	40	mg/L
Ca^{2+}	60	mg/L
Mg^{2+}	9	mg/L

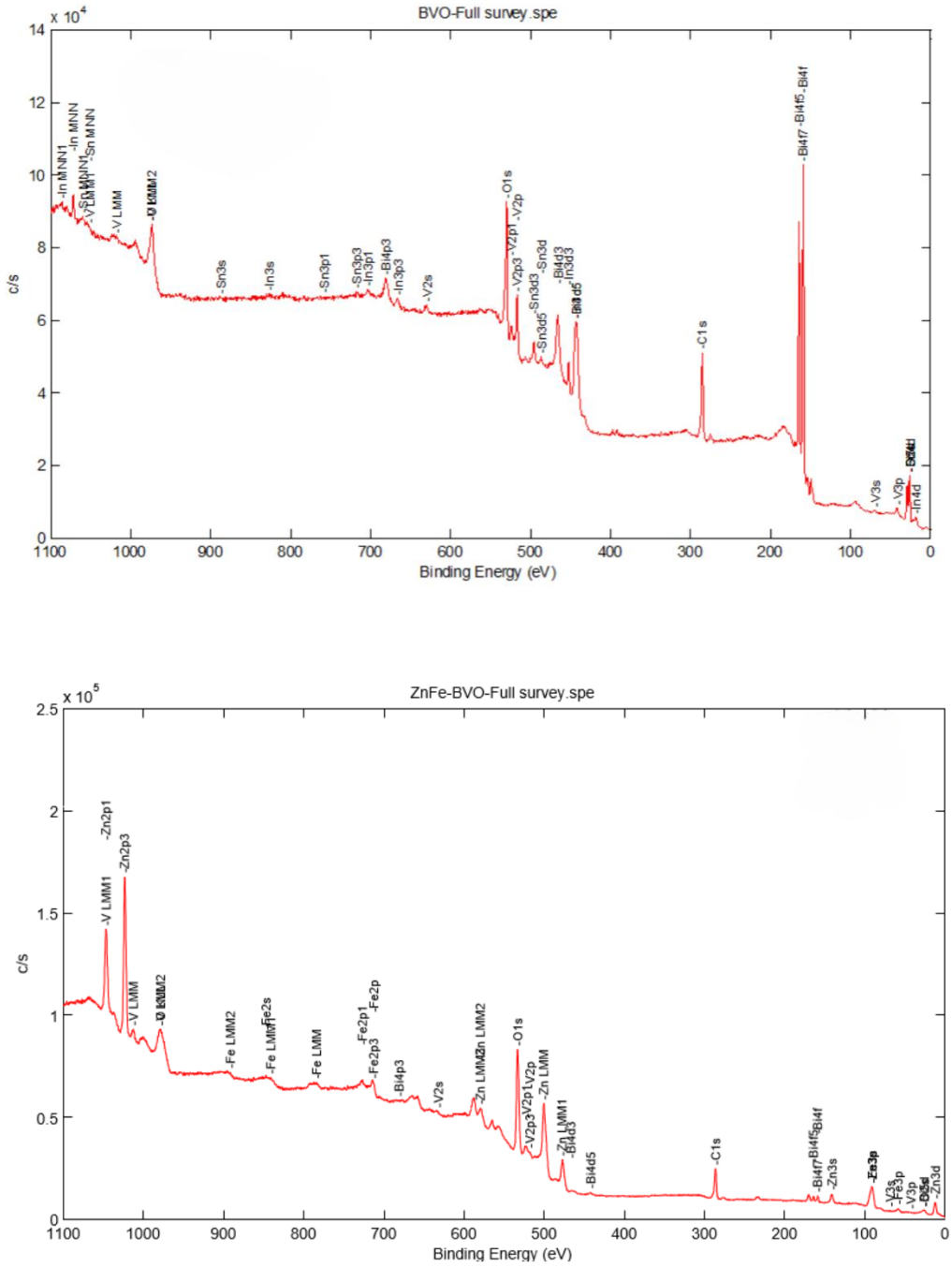


Fig. S1 XPS survey spectra of BVO (A), and ZnFe-LDH/BVO (B).

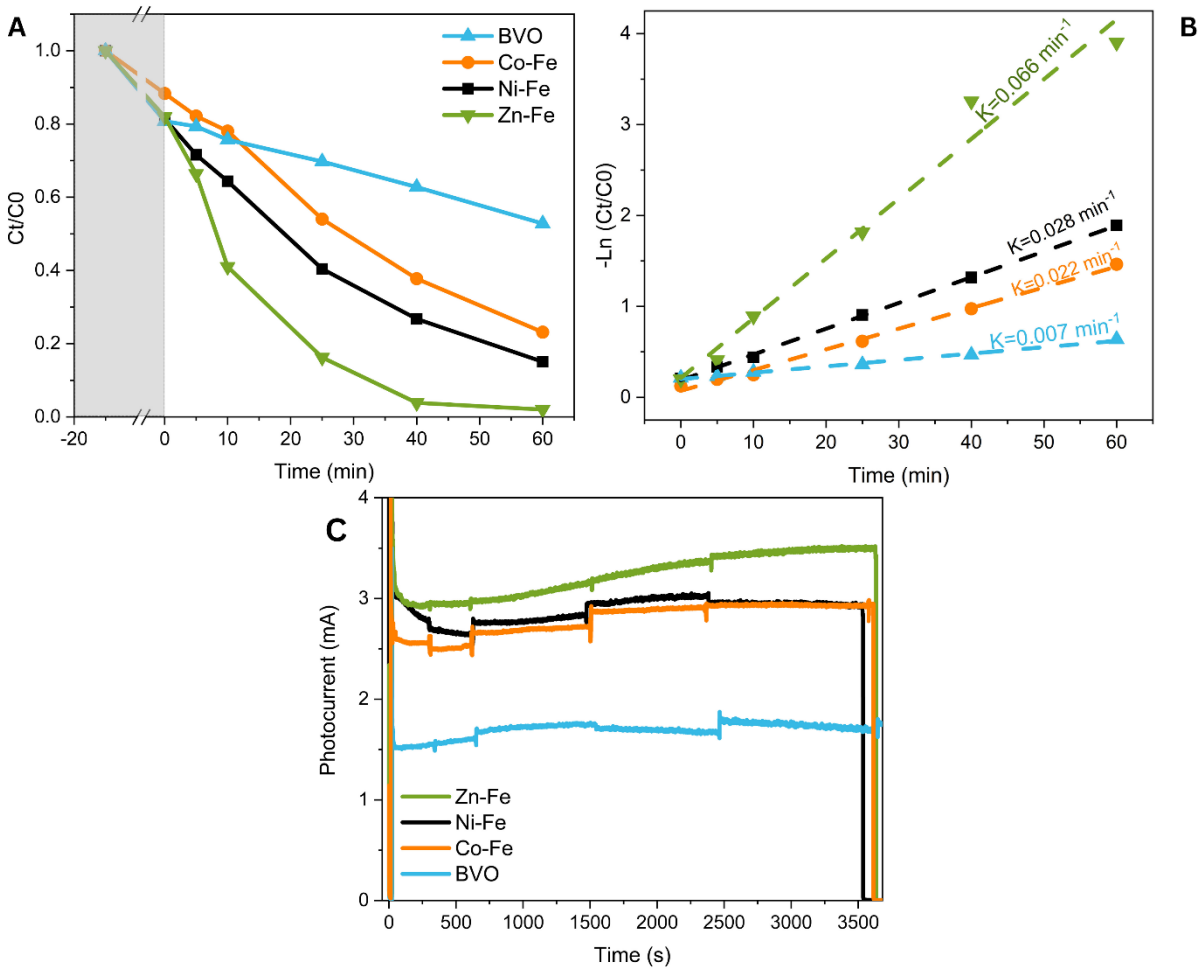


Fig. S2 TC-HCl removal by M-Fe (M= Zn, Ni, Co) LDH/BVO (A), and associated degradation kinetic rate (B), photocurrent during the photoelectrochemical process (C). Experimental condition: TC=10 mg/L, Na_2SO_4=0.02 M, bias potential=1 V vs. Ag/AgCl.

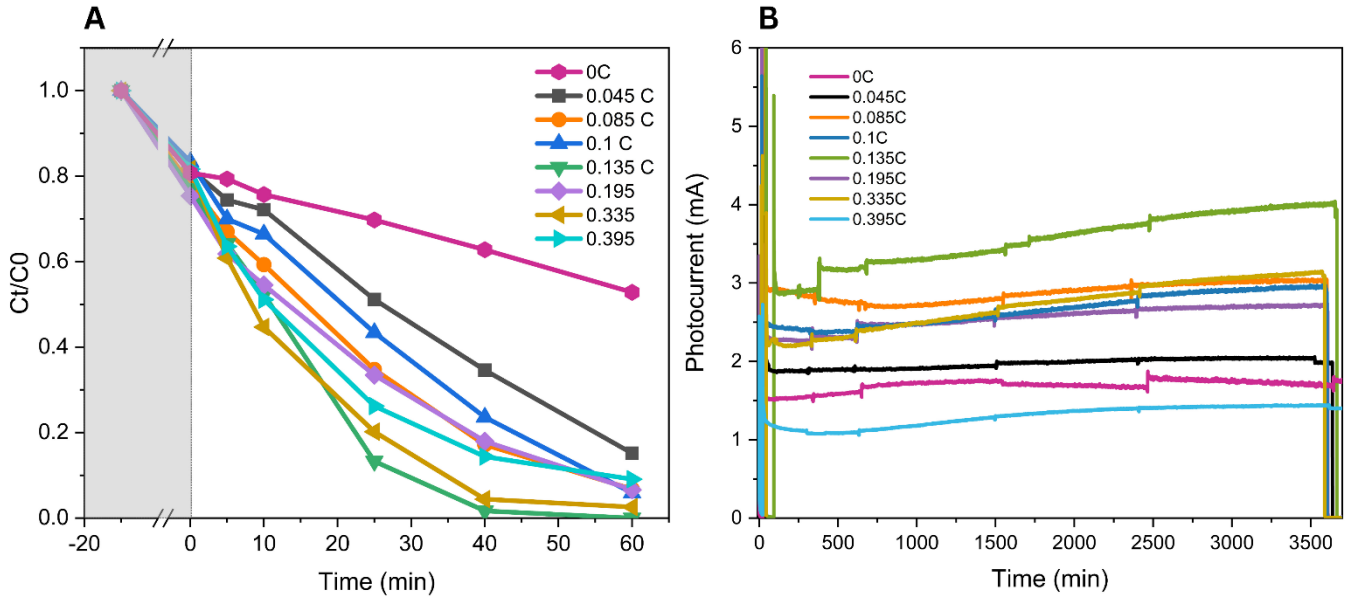


Fig. S3 TC degradation by ZnFe-LDH-XC (X = 0, 0.045, 0.085, 0.1, 0.135, 0.195, 0.335, 0.395)/BVO (A), and associated photocurrents (B). Experimental condition: TC=10 mg/L, Na_2SO_4=0.02 M, bias potential=1 V vs. Ag/AgCl.

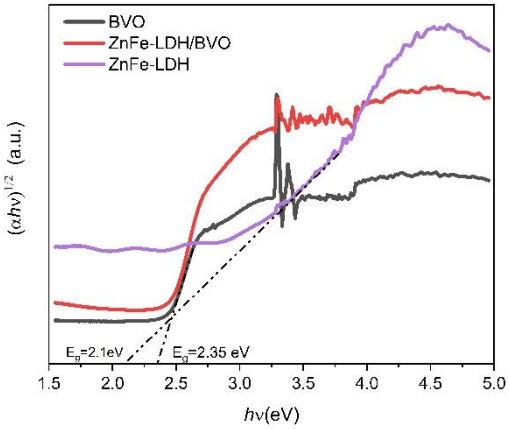


Fig. S4 Tuac plot of the synthesized material using DRS

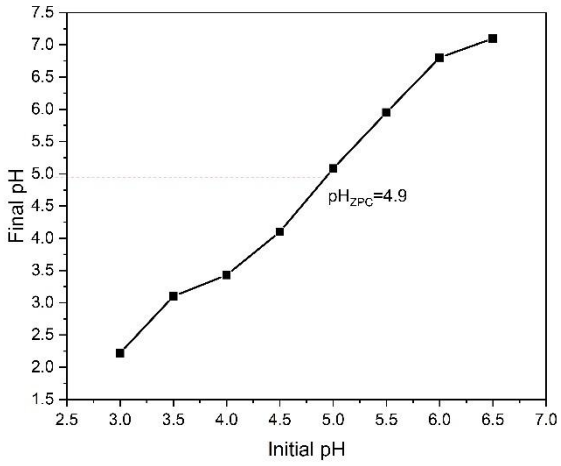


Fig. S5 Zero point charge of ZnFe-LDH/BVO

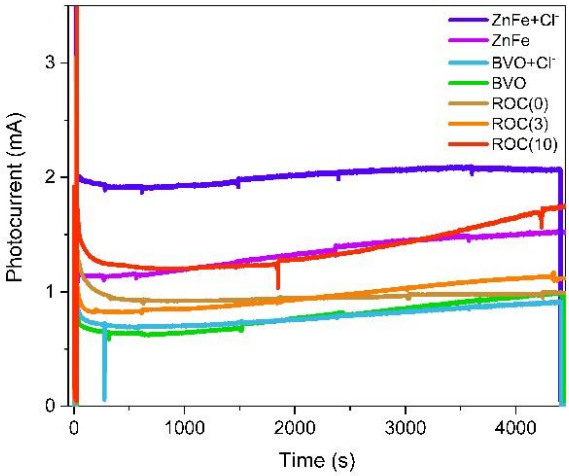


Fig. S6 Photocurrent of ZnFe-LDH/BVO in different solutions

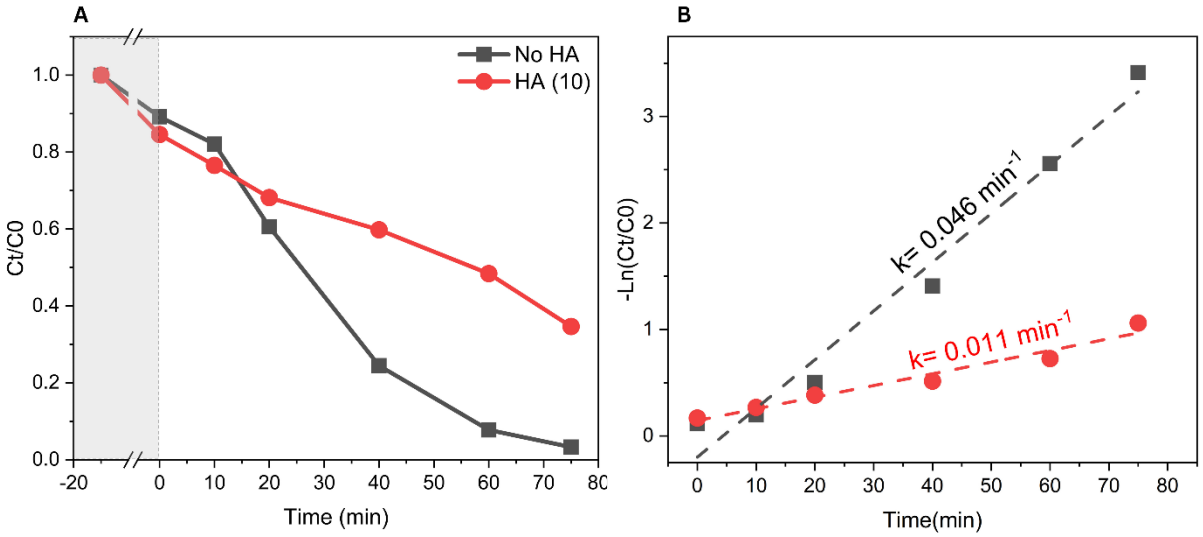


Fig. S7 evaluation of the effect of HA 10 mg/L on the Cl- electrolyte (A), and corresponding kinetic rates (B).

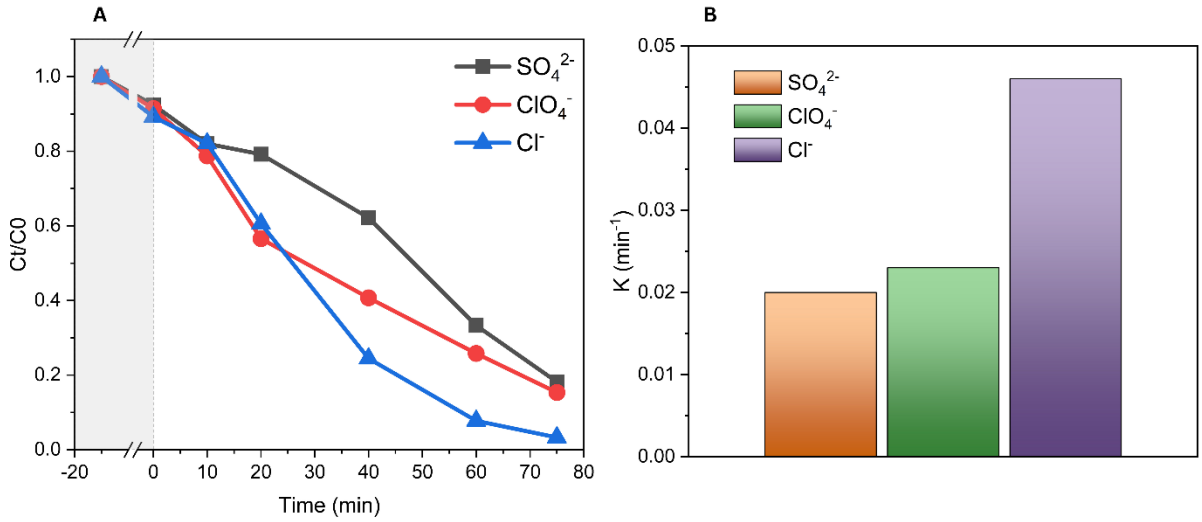


Fig. S8 comparing the effect of ClO_4^- and Cl- on the TC removal (A), kinetic rates (B).

ROSs contribution in TC-HCl removal by ZnFe-LDH/BVO (in sulphate electrolyte)

Several reactive oxygen species (ROS), including $^1O_2$, •OH, and $•O_2^-$, are generated within the PEC system and play a role in TC degradation. Active species scavenging experiments were conducted to determine the contribution of each ROS. Tert-butyl alcohol (TBA) was used to rapidly react with •OH radicals, benzoquinone (BQ) was introduced to scavenge $•O_2^-$ radicals, while L-histidine and ammonium oxalate (AO) were added to remove $^1O_2$ and h^+, respectively. Fig S9A illustrated the degradation patterns of TC with different scavengers, and the contributions of each species are summarized in Fig S9B inset table. The presence of TBA reduced TC degradation from 98% to 66.7%, showing a 31.9% reduction due to the influence of •OH radicals. Similarly, BQ caused a decrease from 98% to 66.5%, indicating a 32.1% reduction, attributed to $•O_2^-$ radicals. The contribution of $^1O_2$ radicals was calculated at 18.9%, while the role of h^+ was the smallest, accounting for 13.7% of the overall degradation. Comparing the kinetic reaction rates, the most significant drop in TC degradation was observed with TBA and BQ, where the rate decreased from 0.066 min^{-1} without scavengers to 0.014 min^{-1} and 0.013 min^{-1} for •OH and $•O_2^-$, respectively, further validating the key role these reactive species play in TC removal.

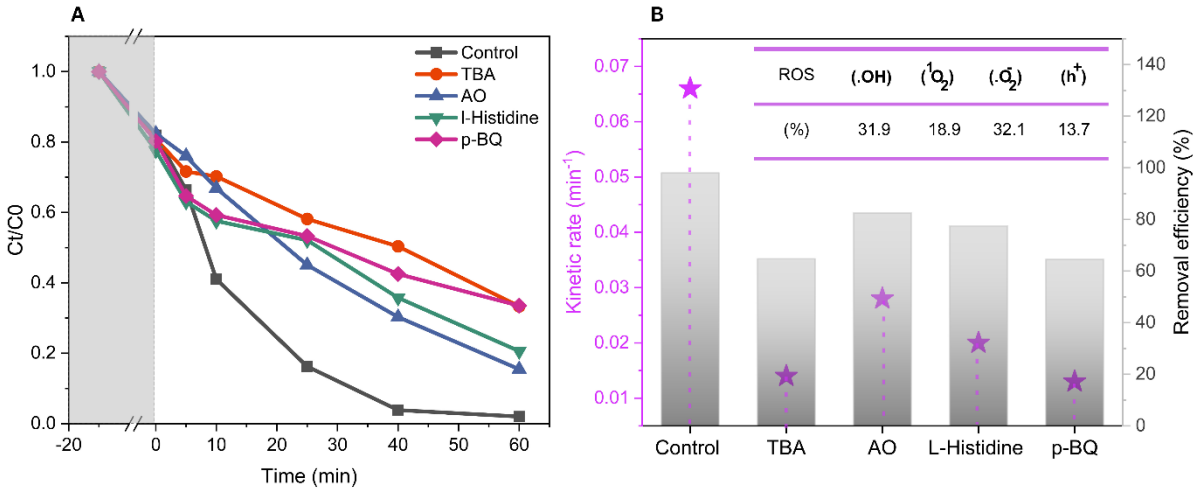


Fig. S9 scavenging experiment for determining ROSs effect on TC removal (A), degradation kinetic rate of the process in the presence of scavengers and ROSs contribution in inset figure (B)

Table S3 RCSs formation reactions

Reaction	Rate constant	No.	Ref.
$Cl^- + h^+ \rightarrow \bullet Cl$		1	(Y. Zhang et al. 2019)
$2Cl^- \rightarrow Cl_2 + 2e^-$		2	(Y. Zhang et al. 2019)
$Cl_2 + H_2O \rightarrow HClO + H^+ + Cl^-$	$k = 2.7 \times 10^{-1}\ M^{-1}s^{-1}$	3	(Y. Zhang et al. 2019)
$Cl^- + 2OH^- \rightarrow OCl^- + H_2O + 2e^-$		4	(Y. Zhang et al. 2019)
$HOCl \rightarrow OCl^- + H^+$	$k = 1.6 \times 10^{3}\ M^{-1}s^{-1}$	5	(Guo et al. 2017)
$HOCl + \bullet Cl \rightarrow \bullet ClO + H^+ + Cl^-$	$k = 3 \times 10^{9}\ M^{-1}s^{-1}$	6	(Minakata, Kamath, and Maetzold 2017)
$HOCl + \bullet OH \rightarrow \bullet ClO + H_2O$	$k = 2 \times 10^{9}\ M^{-1}s^{-1}$	7	(Minakata, Kamath, and Maetzold 2017)
$OCl^- + \bullet Cl \rightarrow \bullet ClO + Cl^-$	$k = 8.2 \times 10^{9}\ M^{-1}s^{-1}$	8	(Minakata, Kamath, and Maetzold 2017)
$OCl^- + \bullet OH \rightarrow \bullet ClO + OH^-$	$k = 8.8 \times 10^{9}\ M^{-1}s^{-1}$	9	(Minakata, Kamath, and Maetzold 2017)
$\bullet Cl_2^- + \bullet Cl_2^- \rightarrow Cl_2 + 2Cl^-$	$k = 6.3 \times 10^{8}\ M^{-1}s^{-1}$	10	(Meghlaoui et al. 2019)

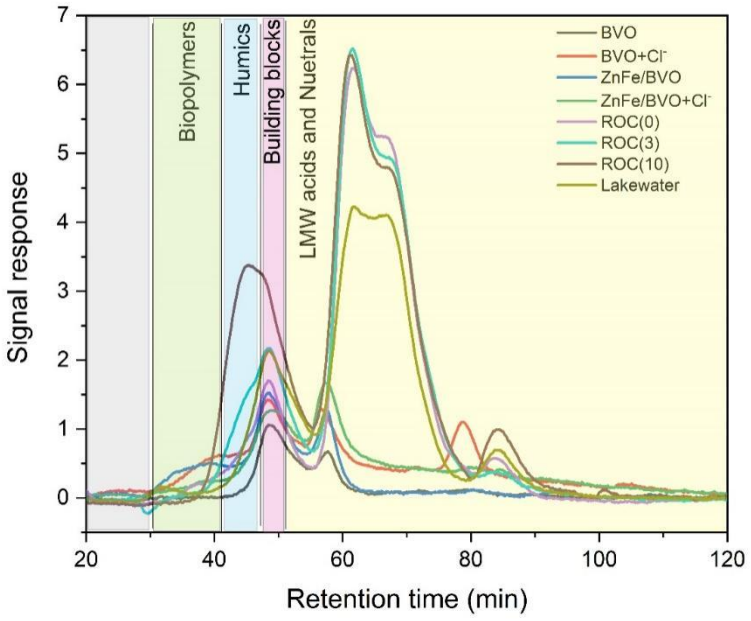


Fig. S10 LC-OCD chromatogram of organic compounds in different solutions after 75 min treatment

DBP control strategies in chlorine-mediated PEC systems:

The following section provides additional complementary strategies that may be adopted to mitigate DBP formation in PEC-Cl systems.

Photoanode/material-side control: reducing secondary halogenation at the interface. Beyond process-train controls (pretreatment/polishing), DBP mitigation can be supported by selecting and engineering photoanodes that steer chlorine activation pathways and limit excessive halogenation. Prior PEC-RCS research has shown that the photoanode identity (e.g., TiO_2 vs WO_3 vs $BiVO_4$) strongly influences reactive chlorine speciation and oxychloride/byproduct tendencies, highlighting that RCS outcomes are material-dependent rather than solely governed by bulk chloride (Li et al. 2021). In addition, recent studies demonstrate that surface engineering of $BiVO_4$ (e.g., vacancy engineering) can tune charge separation and reactive chlorine chemistry, which provides a practical route to improve performance while moderating

undesirable secondary reactions. More broadly, electrochemical oxidation/byproduct reviews emphasize that byproduct control is achievable through electrode/material design that shifts interfacial selectivity (e.g., favoring OER over CER), thereby reducing the formation of chlorinated byproducts and downstream halogenated DBPs (Vos et al. 2019). Accordingly, future optimization of ZnFe-LDH/BVO can incorporate interface/surface modifications aimed at controlling the balance between ROS-dominated oxidation and chlorine-mediated halogenation while retaining the charge-separation benefits of the heterojunction.

Quenching after treatment as an operational safeguard. In practice, residual oxidants can continue reacting after the intended treatment endpoint and may promote additional DBP formation during holding. As a deployment safeguard, rapid quenching of residual oxidants after treatment can prevent post-reaction DBP growth; however, adding scavengers during PEC operation is not recommended because it would compete with pollutant oxidation (Li et al. 2023; Chen et al. 2024).

Operational-condition optimization: bias potential and pH. Prior ROC-PEC work demonstrates that DBP yields can increase substantially at higher anodic potentials due to stronger chlorine activation and increasing free-chlorine contribution, while pH alters DBP profiles by shifting HOCl/OCl^- speciation and the balance of reactive oxidants formed. Accordingly, avoiding unnecessarily high bias and maintaining near-neutral pH (when adjustable) are practical operational levers to reduce DBP risk while maintaining contaminant removal performance (Chen, et al. 2020).

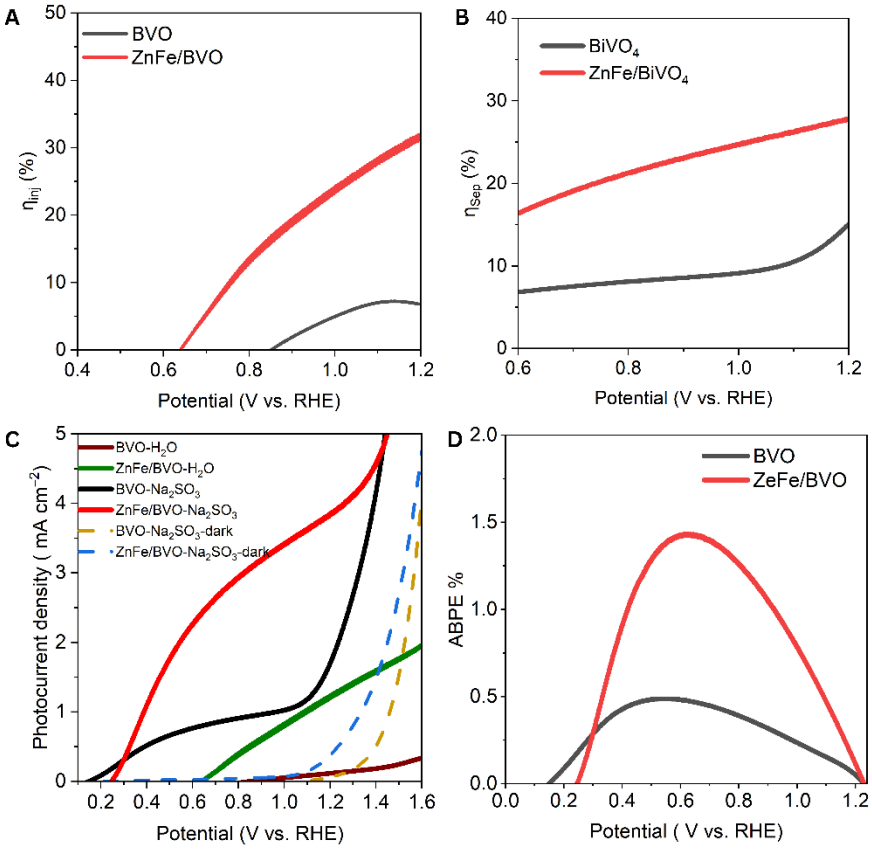


Fig. S11 Injection (A) and separation (B) efficiency, LSV (C), ABPE% (D) graph of BVO and ZnFe-LDH/BVO in the simplified synthetic ROC solution and in presence of Na2SO3 as a hole scavenger.

To further confirm the enhanced charge dynamics in ZnFe-LDH/BVO, we performed the PEC measurements (Figure S11C) in the presence of sodium sulfite as hole scavenger (Na_2SO_3, 0.5 M) to evaluate the charge injection, η_{inj} and separation efficiency, η_{sep}. Here, η_{inj} denotes the fraction of photogenerated holes injected from $BiVO_4$ into the electrolyte for water oxidation, while η_{sep} represents the fraction of holes that reach the photoanode/electrolyte interface without recombining in the bulk. As shown in Figure S11A-B, coupling $BiVO_4$ with ZnFe-LDH significantly enhances the charge transfer by increasing the injection efficiency from 5% to 30% at 1.23 V vs. RHE while increases the separation efficiency from 15% to 25%. These enhancements confirm the effective suppression of charge carrier recombination, thereby accelerating the water oxidation kinetics and improving the hydrogen

production. In the absence of Na_2SO_3, the photocurrent of $BiVO_4$ was low due to the surface recombination. While the photocurrent is significantly increased in the presence of Na_2SO_3, due to the suppression of surface recombination. Additionally, the ABPE% experiences a notable enhancement, increasing from 0.2% to 1.4% when Na_2SO_3 is applied (S11D).

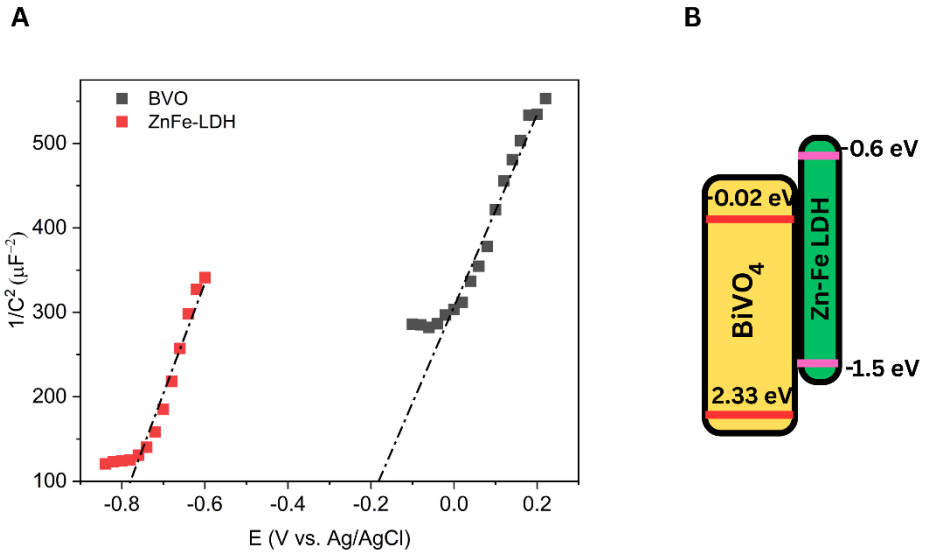


Fig. S12 Mott-Schottky plot of BVO and Zn-Fe LDH at frequency of 2000 Hz (A), and band alignment of ZnFe-LDH/BVO heterojunction (B).

References

Chen C Z, Zhao X T, Chen H R, Wang J J, Wang Y T, Xian Q M (2024). The investigation of quenching conditions for the analysis of total organic halogen, aliphatic and aromatic halo-genated disinfection byproducts formed from chlor(am)ination. Journal of Hazardous Materials, 475: 134918

Chen Y W, Li S, Hu J Y (2020). Photoelectrocatalytic degradation of organics and formation of disinfection byproducts in reverse osmosis concentrate. Water Research, 168: 115105

Guo K H, Wu Z H, Shang C, Yao B, Hou S D, Yang X, Song W H, Fang J Y (2017). Radical chemistry and structural relationships of PPCP degradation by UV/chlorine

treatment in simulated drinking water. Environmental Science & Technology, 51(18): 10431–10439

Li X, Zhao Z J, Qu Z, Li X Y, Zhang Z L, Liang X J, Chen J S, Li J F (2023). A review of traditional and emerging residual chlorine quenchers on disinfection by-products: impact and mechanisms. Toxics, 11(5): 410

Luo X F, Zhu S M, Wang J, Sun J L, Bu L J, Zhou S Q (2020). Formation, speciation and toxicity of CX3R-type disinfection by-products (DBPs) from chlor(am)ination of 2, 4-diaminobutyricacid (DAB). Ecotoxicology and Environmental Safety, 191: 110247

Minakata D, Kamath D, Maetzold S (2017). Mechanistic insight into the reactivity of chlorine-derived radicals in the aqueous-phase UV–chlorine advanced oxidation process: quantum mechanical calculations. Environmental Science & Technology, 51(12): 6918–6926

Plewa M J, Simmons J E, Richardson S D, Wagner E D (2010). Mammalian cell cytotoxicity and genotoxicity of the haloacetic acids, a major class of drinking water disinfection by-Products .Environmental and Molecular Mutagenesis, 51(8−9): 871–878

Vos J G, Liu Z C, Speck F D, Perini N, Fu W T, Cherevko S, Koper M T M (2019). Selectivity trends between oxygen evolution and chlorine evolution on iridium-based double perovskites in acidic media. ACS Catalysis, 9(9): 8561–8574

Xiang H M, Shao Y S, Gao N Y, Lu X, An N, Chu W H (2020). Removal of β-cyclocitral by UV/persulfate and UV/chlorine process: degradation kinetics and DBPs formation. Chemical Engineering Journal, 382: 122659

Zohra Meghlaoui F, Merouani S, Hamdaoui O, Bouhelassa M,Ashokkumar M (2019). Rapid catalytic degradation of refractory textile dyes in Fe(II)/chlorine system at near neutral PH: radical mechanism involving chlorine radical anion (Cl^{2-})-Mediated transformation pathways and impact of environmental matrices. Separation and Purification Technology, 227: 115685